PNAS RESEARCH ARTICLE | EARTH, ATMOSPHERIC, AND PLANETARY SCIENCES

Dynamical constraints on the vertical structure of Jupiter's polar cyclones

Nimrod Gavriel[a,1] and Yohai Kaspi[a]

Edited by Francis Nimmo, University of California, Santa Cruz, CA; received February 19, 2025; accepted September 16, 2025

Jupiter's poles feature striking polygons of cyclones that drift westward over time, a motion governed by β-drift (vortex motion caused by the latitudinal variation of the Coriolis force). This study investigates how β-drift and the resulting westward motion depend on the depth of these cyclones. Counterintuitively, shallower cyclones drift more slowly, a consequence of stronger vortex stretching. By employing a 2D quasi-geostrophic model of Jupiter's polar regions, we constrain the cyclones' deformation radius, a key parameter that serves as a proxy for their vertical extent, required to replicate the observed westward drift. We then explore possible vertical structures and the static stability of the poles by solving the eigenvalue problem that links the 2D model to a 3D framework, matching the constrained deformation radius. These findings provide a foundation for interpreting upcoming Juno microwave measurements of Jupiter's north pole, offering insights into the static stability and vertical structure of the polar cyclones. Thus, by leveraging long-term motion as a constraint on vertical dynamics, this work sets the stage for advancing our understanding of the formation and evolution of Jupiter's enigmatic polar cyclones.

Jupiter | polar vortices | vertical stability | the Juno mission | microwave radiometer

Significance

Jupiter's poles feature clusters of large, long-lasting cyclones that slowly drift westward. We argue that the depth to which these cyclones extend below the cloud layers significantly influences this drift rate. By comparing computer simulations with observations, we estimate the depth of the cyclones and shed light on the stability of Jupiter's atmosphere at high latitudes. These insights are particularly critical for Juno's extended mission, which now allows the Microwave Radiometer to observe these cyclones with unprecedented resolution, providing a direct test of our framework and facilitating quantitative interpretation of their vertical structure. Our results directly support this new phase of the Juno mission, offering key constraints to understand the formation, persistence, and dynamics of these giant polar storms.

Historically, our understanding of Jupiter's atmosphere has been limited to observations of its visible cloud layer, located near the 1-bar pressure level. This limitation arises from the challenges of probing beneath the optically thick ammonia and water clouds (1, 2). Until recently, the only direct measurements of Jupiter's subcloud layers were the localized and costly in-situ data collected by the Galileo Probe (3). However, an indirect method using gravity measurements (by tracking changes in the Juno spacecraft's acceleration during close flybys) has enabled insights into the large-scale flows at depth. This approach has revealed the 3D structure of zonal flows within Jupiter's subequatorial jet streams (4–6) and constrained the depth of the Great Red Spot (GRS) to less than 500 km (7, 8).

Another approach to exploring Jupiter's subcloud layers involves observations at cloud-penetrating frequencies. For example, using radio frequencies, the Earth-based Very Large Array telescopes have probed down to pressures of approximately 8 bars (2). The Juno Microwave Radiometer (MWR) offers an enhanced use of cloud-penetrating frequencies, leveraging its orbital proximity to achieve deeper measurements with finer spatial resolution. Equipped with six channels, the MWR has been providing spatially resolved observations of brightness temperature down to depths of approximately 240 bars (9, 10). These thermodynamic measurements are influenced both by temperature variations (11) and the opacity of ammonia clouds (12). Although there is ongoing debate about the relative contributions of these factors, the observed deep patterns reveal valuable information about the vertical structure and depth of atmospheric phenomena seen at the cloud tops. For example, the MWR detected alternating zonal bands of ammonia depletion and enrichment extending to 240 bars between midlatitude jets. These patterns correspond to the upwelling and downwelling branches expected in a Ferrel-cell-like circulation (13, 14).

Another key instrument on Juno, the Jovian Infrared Auroral Mapper (JIRAM), was designed to study the aurora and atmospheric chemistry at 5 to 7 bar (15). During Juno's polar orbits, as JIRAM is insensitive to half the pole being dark and can wholly observe the pole, it discovered a new phenomenon: a polar "crystal" of massive cyclones (each ~5,000 km wide) inhabiting each pole, consisting of a polar cyclone (PC) and 8 circumpolar cyclones (CPCs) at the north pole, and 5 at the south (16). The MWR instrument, designed to function optimally at the shorter distances from Jupiter's cloud-tops during the around-equatorial skims in its original polar orbit, now enters a phase in Juno's extended mission, where the orbit has considerably shifted, allowing MWR measurements near the north pole of Jupiter (17). This enables multichannel measurements with sufficient resolution to capture the north polar cyclones, similar to analogous previous

Author affiliations: [a]Department of Earth and Planetary Sciences, Weizmann Institute of Science, Rehovot 7610001, Israel

Author contributions: N.G. and Y.K. designed research; N.G. performed research; N.G. analyzed data; and N.G. and Y.K. wrote the paper.

The authors declare no competing interest.

This article is a PNAS Direct Submission.

[1]To whom correspondence may be addressed. Email: nimrod.gavriel@weizmann.ac.il.

This article contains supporting information online at https://www.pnas.org/lookup/suppl/doi:10.1073/pnas.2503737122/-/DCSupplemental.

Published October 28, 2025.

measurements of vortices in the midlatitudes (18). This study aims to provide a theoretical framework for interpreting the upcoming MWR observations of Jupiter's north pole, offering predictions about the vertical structure and extent of the polar cyclones.

Jupiter's Polar Cyclones. The energetic processes sustaining Jupiter's polar cyclone configurations, while explored in prior studies (19–23), remain largely unconstrained. Nevertheless, substantial progress has been made in understanding the principal momentum balance that governs these cyclones, explaining both their stability and long-term motion. This momentum balance is closely related to the concept of β-drift, a secondary effect that causes vortices to move due to their interaction with a background vorticity gradient (24) known to influence the motion of tropical cyclones on Earth (25). The phenomenon of β-drift has been explored extensively in idealized settings, including theoretical studies (26, 27), numerical simulations (28, 29), and laboratory experiments (30–34).

Traditionally, as suggested by the term "β-drift," studies have focused on the interaction of cyclones with β, the meridional gradient of the planetary vorticity f, causing a poleward-westward migration through the generation of opposite vorticity anomalies (usually termed β-gyres) surrounding the core. However, in addition to β, cyclones on Jupiter's poles exhibit mutual repulsion due to the interaction of the vorticity gradient of one cyclone with the velocity field of another. This mutual interaction allows for the stable crystal-like configuration of the cyclones (35), provided that they are surrounded by an anticyclonic annulus, commonly referred to as shielding (36). This repulsion also explains the oscillatory motion of the polar cyclones (37), as observed by Juno (38).

Beyond oscillatory motion, the cyclones exhibit a mean westward drift, with rates of approximately 3° and 7° per year at the north and south poles, respectively (39, 40). This westward drift arises from the β-drift acting collectively on the group of cyclones. By adopting a "center of mass" perspective, the mutual interactions between the cyclones are effectively averaged out, leaving only the cumulative interaction of the group with β. This dynamic leads to a group oscillation around the poles accompanied by a westward precession, manifesting as the observed drift (29).

In this study, we investigate how the vertical structure and depth of Jupiter's polar cyclones influence their mean westward drift. First, we employ an idealized 2D model to explore how depth, and the associated column stretching, affects β-drift on a vortex in a β-plane. Next, we perform a parameter scan using a 2D Quasi-Geostrophic (QG) polar model with Jupiter's polar cyclones initialized in the system to constrain the QG deformation radius (L_d), a proxy for depth, such that the modeled westward drift matches observational data. Finally, we solve the eigenvalue problem posed by comparing 2D and 3D QG systems to deduce the vertical structures and static stability of the polar cyclones based on the constrained L_d.

The Impact of Vertical Depth on Vortex β-Drift

A standard framework for understanding the motion of vortices due to β-drift is the barotropic QG equation of a seeded vortex on a β-plane (24, 27, 41). In this formulation, cyclones undergo poleward-westward propagation in a planetary β, with the drift amplitude scaling with the dimensionless parameter $\hat{\beta} = \frac{\beta R^2}{V}$ (29, 42), where R and V are the characteristic size and velocity of the cyclone. In this section, we seek to understand how the vertical extent (through stretching) modifies the classical β-drift by adding the stretching term to the QG equation, before treating other important complexities such as vortex–vortex interactions. Stretching, in this context, refers to the vertical elongation (or compression) of a fluid column accompanied by horizontal convergence (or divergence). In QG dynamics, such vertical motions alter the potential vorticity (PV) by concentrating or diluting the background vorticity (see *SI Appendix*, Fig. S1 and the accompanying text for more intuition).

Following the derivation in ref. 27 but including stretching (see *SI Appendix* for scaling, derivation, and other details), we develop the equations in a reference frame moving with the center of the cyclone. The scaled resulting QG equation becomes (focusing on the dominant terms)

$$\frac{\partial}{\partial t}\left(\xi_g - \frac{\psi_g}{\mathrm{Bu}}\right) = -\hat{\beta} v_v - \mathbf{u}_v \cdot \nabla \xi_g, \qquad [1]$$

where ξ and ψ are the vorticity and streamfunction, respectively, and $\mathbf{u} = (u, v)$ is the velocity vector. Subscripts v and g represent, respectively, a constant background vortex flow and a "generated" field leading to the β-drift. The Burger number, $\mathrm{Bu} \equiv \left(\frac{L_d}{R}\right)^2$, incorporates the effect of the deformation radius, $L_d = \frac{\sqrt{gH}}{f_0}$, where g is gravitational acceleration, H is the layer depth, and f_0 is the Coriolis parameter. The term $-\frac{\partial}{\partial t}\left(\frac{\psi_g}{\mathrm{Bu}}\right)$ captures the influence of stretching in the single-layer QG model.

The model is solved for vortex profiles of the dimensional form (43):

$$\xi_v = \frac{V}{R}\left(2 - \left(\frac{r_c}{R}\right)^b\right)\exp\left[\frac{1}{b}\left(1 - \left(\frac{r_c}{R}\right)^b\right)\right], \qquad [2]$$

where r_c is the distance from the vortex's center, and b is a shape factor that controls the sharpness and shielding of the vortex profile. For a more detailed analysis of the role of b, see ref. 36. The initial-value problem is solved using the Dedalus PDE solver (44). The results from this model, as a function of Bu, are shown in Fig. 1. The zonal β-drift velocity, defined as $u_\beta \equiv u_g|_{(x=0,\ y=0)}$, displays an exponential relaxation with time, which is modeled by $\mathrm{U}_\beta\left(1 - e^{-t/\tau}\right)$ (Fig. 1*A*), a parameterization that provides a good fit for $\mathrm{Bu} \lesssim 5$.

We further examine the dependence of the fitted maximum drift velocity (U_β) and timescale (τ) on layer depth (Fig. 1*C*) for three values of the shape factor b within a physically relevant range. The results indicate that while the drift amplitude is relatively insensitive to changes in b, it becomes more negative (more strongly westward) as the Burger number increases (or equivalently, as H increases).

In Gavriel and Kaspi (29) (their Fig. 2), the layer depth H is assumed to be infinite, which implies $L_d \to \infty$ and $\mathrm{Bu} \to \infty$, effectively removing the stretching term from Eq. **1**. This assumption highlights that for very deep layers, any change in the fluid upper surface height (δh) is negligible compared to the total depth ($\frac{\delta h}{H} \ll 1$), rendering stretching effects unimportant to the dynamics.

However, when H (and thus Bu) is finite, the PV anomaly generated by the β-effect (the term $-\hat{\beta} v_v$) is divided between two parts: the formation of β-gyres (through $\frac{\partial \xi_g}{\partial t}$) and column stretching (through $-\frac{\partial}{\partial t}\frac{\psi_g}{\mathrm{Bu}}$). As stretching has more relative significance in shallower layers, it claims a larger share of the

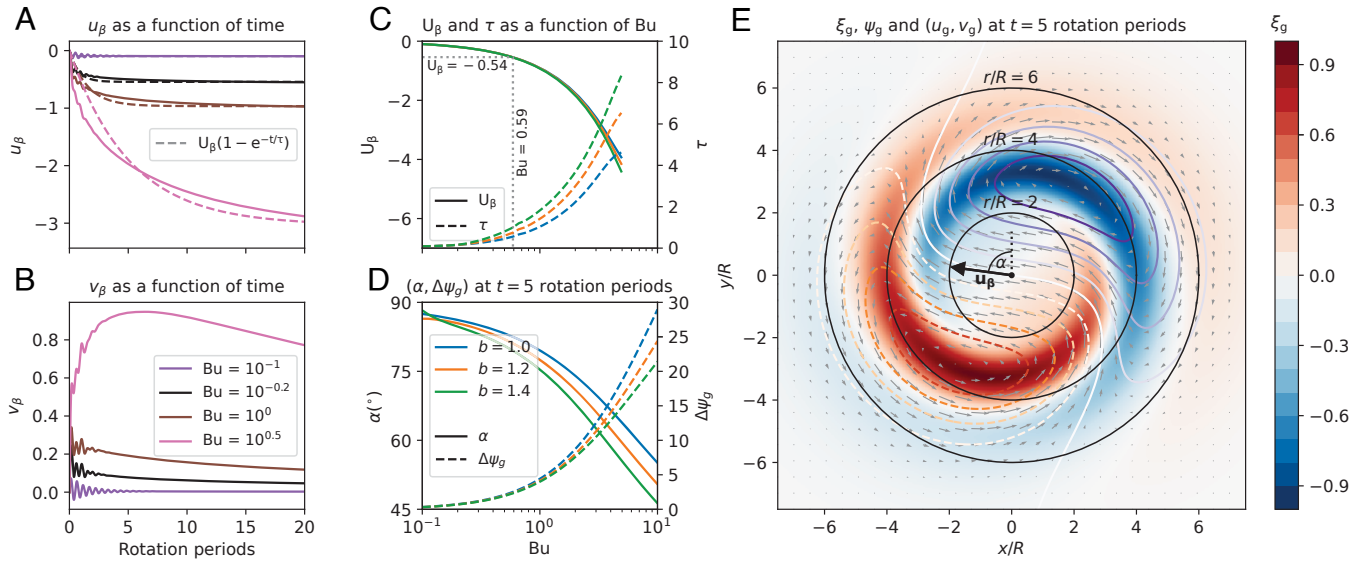

Fig. 1. Impact of stretching on β-drift dynamics in a single-layer QG framework: A single cyclone on a β-plane. (*A* and *B*) Evolution of the zonal (u_β) and meridional (v_β) drift velocities over time for four different values of the Burger number and $b = 1.2$. Dashed curves show exponential fits with amplitude U_β and timescale τ. Here, (u_β, v_β) are nondimensional, scaled by $\hat{\beta}\hat{V}$. (*C*) Plots of U_β (solid line, *Left* axis) and τ (dashed line, *Right* axis, in rotation periods) as functions of Bu for three values of the shape factor b (legend in panel *D*). The exponential parameterization becomes inadequate for Bu $\gtrsim 5$ (*SI Appendix*, Fig. S2). (*D*) Solid line: Phase angle α (defined in panel *E*) between u_β and v_β as a function of Bu. Dashed line: Strength of the β-gyres, quantified as $\Delta\psi_g = \max(\psi_g) - \min(\psi_g)$, with values nondimensionalized by $\hat{\beta}R\hat{V}$. (*E*) The vorticity field (ξ_g, in color), stream function (ψ_g, in contours), and velocity field ($\mathbf{u}_g$, arrows) after five rotation periods for Bu $= 0.59$ and $b = 1.2$. The β-gyres appear as red and blue lobes surrounding the cyclone core. The color bar represents the scaled (by $\hat{\beta}\hat{V}/R$) vorticity field. See Movie S1 for the simulation.

total PV response, thereby weakening the β-gyres. This trend is reflected in Fig. 1*C*, where shallower layers correlate with stronger stretching and hence smaller β-drift velocities. This reduction is also evident in Fig. 1*D*, where the difference between the extreme streamfunction values of the β-gyres, $\Delta\psi_g$, becomes smaller.

Using the Jovian values for the north and south poles of $\hat{\beta}$, R, and V from ref. 29, we find that matching the observed westward drift corresponds to $U_\beta = -0.46$ for the north pole and $U_\beta = -0.54$ for the south pole, marked in Fig. 1*C*. These values correspond to Bu $= 0.49$ for the north pole and Bu $= 0.59$ for the south, which is used in Fig. 1*E* to show the generated fields after five rotation periods. The influence of Bu extends beyond the reduction of the β-drift amplitude. Smaller Bu values also reduce the time required to reach the peak drift velocity (τ in Fig. 1*C*) and lead to a more zonally directed drift overall (α in Fig. 1*D*).

From Bu $= (0.49, 0.59)$ and $R = (811, 861)$ km (29), the resulting deformation radii are $L_d = (568, 658)$ km for the north and south poles, respectively. These values should not be interpreted as definitive physical estimates, but rather as outcomes of an idealized model that omits vortex–vortex interactions and the polar variation of f. Instead, this simplified framework is meant to provide insight into the role of stretching alone in modulating β-drift. In the next section, we consider these additional complexities to derive more realistic values of L_d needed to match the observed drift rates.

Estimating the Deformation Radius Using a Single-Layer QG Model of the Jovian Poles

While the previous section focused on how vertical extent modifies β-drift, the idealized model used there does not provide a realistic estimate of L_d. To address this limitation, we now present a single-layer QG model initialized with a polar vortex crystal. This model evolves under the full spherical form of the vertical component of Jupiter's rotation rate, $f = 2\Omega\cos\left(\frac{r}{R_J}\right)$, where Ω is Jupiter's rotation rate, R_J is Jupiter's radius, and r is the distance from the pole. We use Dedalus (44) to solve the polar QG equation (46):

$$\frac{D}{Dt}\left(\nabla^2\psi + 2\Omega\cos\left(\frac{r}{R_J}\right) - \frac{1}{L_d^2}\psi\right) = 0, \qquad [3]$$

with multiple cyclones prescribed by Eq. **2**, with one PC and eight (five) CPCs placed initially at the observed locations during Juno's PJ4 orbit for the north (south) poles (Fig. 2 *A* and *B*). For simplicity and because of limited observational data, we assume identical cyclones. Due to this choice and the absence of small-scale forcing, the oscillatory motion discussed by Gavriel and Kaspi (37) is not excited. Hence, we focus on reproducing the mean westward drift. While zonal jets could, in principle, influence the drift, no such flows have been observed in the vicinity of the cyclones (47). Moreover, JunoCam imagery is consistent with a two-dimensional, isotropic turbulent regime (48), and thus zonal flows are not included in this model.

This model involves four unknown parameters: L_d, and the three cyclone profile parameters (R, V, b). To explore the phase space of this model, we use the Ultranest library (45), which employs a Bayesian nested sampling approach to identify the best-fitting solutions (49). As a benchmark, we use the 5-y observed trajectories of the north and south polar cyclones (40) (Fig. 2 *A* and *B*) to calculate the average westward drift between the cyclones. This value is then used to calculate a likelihood function that evaluates the probability of a parameter set being accurate, based on the resultant model westward drift (see *SI Appendix* for details on the numerical model, likelihood function, and model sampling).

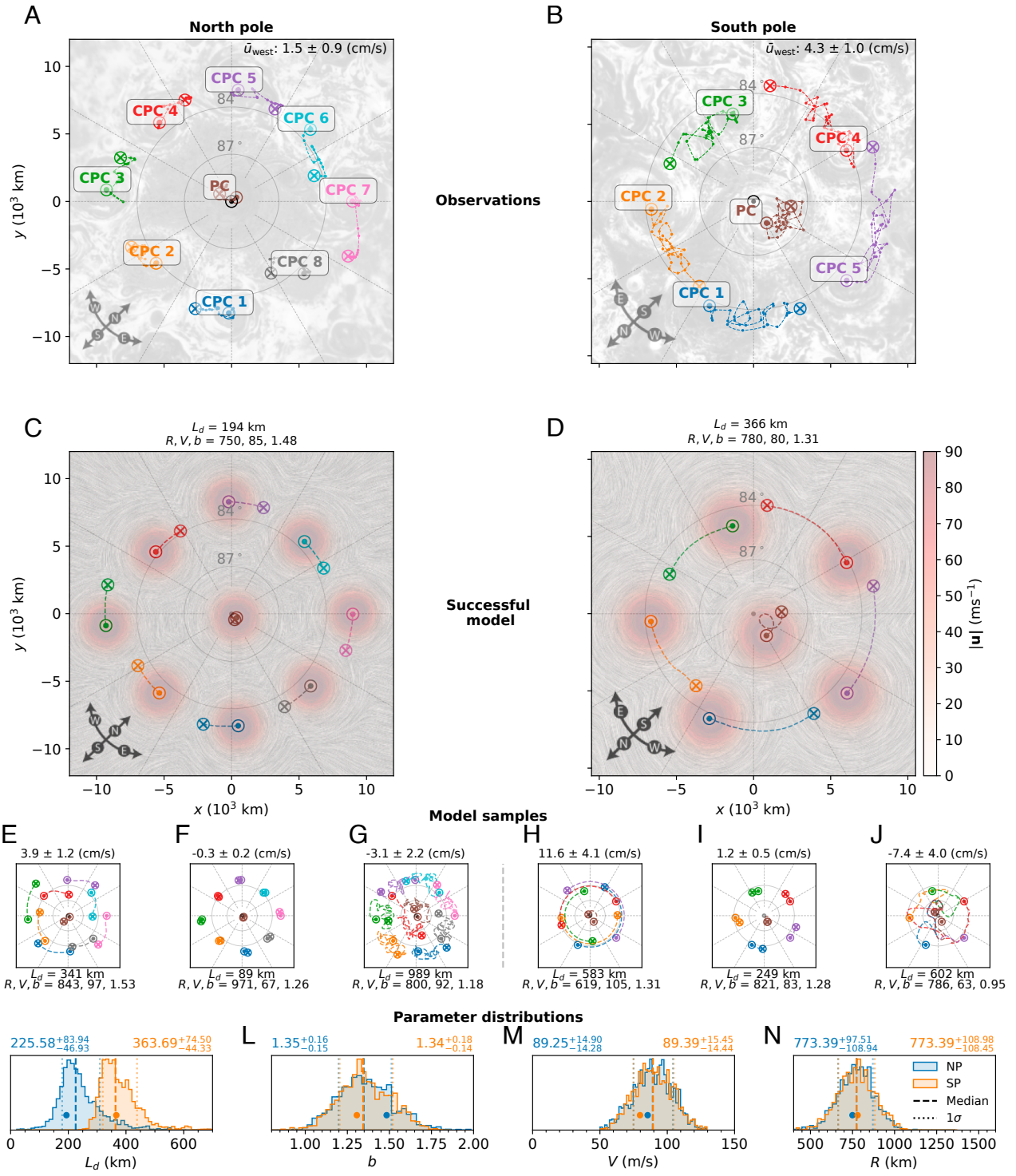

Fig. 2. Constraining L_d at Jupiter's poles using observed and simulated cyclone drifts. (*A* and *B*) Observed trajectories of the north (*A*) and south (*B*) polar cyclones over five years (40). The symbols ⊙ and ⊗ mark the start and end points, respectively. The background is a JIRAM infrared image from PJ4 (Image from ref. 16), corresponding to the onset of these trajectories. (*C* and *D*) Simulated trajectories after five years for a model that reproduces the observed mean westward drift. See Movie S2 and Movie S3 for animations of panels *C* and *D*, respectively. The color scale indicates the magnitude of the velocity vector, while the streaks represent the flow direction through line integral convolution of the velocity field at $t = 0$. (*E*–*J*) Sample model trajectories from the nested sampling routine, illustrating diverse outcomes. The numbers above the panels are the mean and SD (between the cyclones) of the westward drift. The parameters used in each panel are listed below the panels. (*K*–*N*) Histogram plots of the posterior parameter distributions produced by Ultranest (45), after sampling 15,000 parameter sets per pole for the north (blue) and south (orange) polar cyclones. The dashed lines denote the median, and the dotted lines mark $\pm 1\sigma$ for the distributions. These values are written above the panels. Markers represent the parameter values of the successful models (*C* and *D*). For a corner plot of the joint posterior distributions, see *SI Appendix*, Fig. S4.

We sampled 15,000 parameter sets for each pole, integrating each simulation for seven years and calculating the resultant mean westward drift between the cyclones during the last five years (where the first 2 y act as a spin-up). Illustrative model outputs [Fig. 2 panels (*E*–*G*) for the north pole and panels (*H*–*J*) for the south] span a variety of outcomes: drifts too fast (*E* and *H*),

too slow (F and I), eastward (G), and mergers (J). Examples of parameter sets that successfully recreate the observed drift are shown in Fig. 2 C and D.

Due to intrinsic parameter degeneracies, the algorithm returns a posterior distribution rather than a specific set of parameters that matches the observed westward drift. From this distribution, we obtain a more realistic estimate for the deformation radius of $L_d = 225.58^{+83.94}_{-46.93}$ km and $L_d = 363.69^{+74.50}_{-44.33}$ km at the 1σ confidence level for the north and south poles (Fig. 2K), respectively. The resulting posterior distributions for R, V, and b (Fig. 2 L–N) align well with plausible mean values for Jupiter's polar cyclones, as estimated from cloud feature tracking at the poles (50).

Interpreting the Vertical Structure of Jupiter's Polar Atmosphere from the Drift Rate of the Polar Cyclones

The standard shallow-water (SW) expression for the deformation radius, $L_d = \sqrt{gH}/f_0$, is not well-suited to Jupiter's upper atmosphere. This expression assumes a constant density and no vertical dependence of the flow, whereas Jupiter's upper-atmospheric density increases exponentially with depth (51) over many scale heights. To account for these vertical variations, we consider the continuously stratified QG vorticity equation (46):

$$\frac{D}{Dt}\left(\nabla^2\psi + f + \frac{f_0^2}{\tilde{\rho}}\frac{\partial}{\partial z}\left(\frac{\tilde{\rho}}{N^2}\frac{\partial\psi}{\partial z}\right)\right) = 0, \qquad [4]$$

where N is the Brunt-Väisälä frequency, indicating the stability of the atmosphere with respect to vertical motion, and $\tilde{\rho}$ is the vertical density profile.

To account for variations in the vertical direction, we assume the streamfunction can be separated into horizontal and vertical components:

$$\psi(x, y, z, t) = \sum_n \psi_n(x, y, t)\Phi_n(z), \qquad [5]$$

where $\Phi_n(z)$ is the vertical profile for each n. Substituting this form into the QG equations requires each Φ_n to satisfy the vertical eigenvalue problem (52):

$$\frac{f_0^2}{\tilde{\rho}}\frac{\partial}{\partial z}\left(\frac{\tilde{\rho}}{N^2}\frac{\partial\Phi_n}{\partial z}\right) + \Gamma_n\Phi_n = 0, \qquad [6]$$

where Γ_n is an eigenvalue. For each mode n, the corresponding deformation radius is given by $L_{d,(n)} = \Gamma_n^{-\frac{1}{2}}$ (see *SI Appendix* for the full derivation). Assuming that the cyclones are dominated by a single vertical mode, the horizontal dynamics derived from the two-dimensional QG equation (Eq. **3**), and the three-dimensional QG equation (Eq. **4**) will yield similar results for the given $L_{d,(n)}$; the linearized dynamics are identical (*SI Appendix*). Given our estimates of the L_d values required to achieve the observed westward drift (Fig. 2), we can use the eigenvalue problem posed by Eq. **6** to investigate which vertical structures [eigenfunctions $\Phi_n(z)$] satisfy the required L_d.

We solve this eigenvalue problem using the Dedalus library (44), applying boundary conditions of no vertical velocity at the tropopause ($\partial_z\Phi_n|_{z=0} = 0$) and no flow at the bottom ($\Phi_n|_{z=-H} = 0$). For $\tilde{\rho}(z)$, we adopt a reference density profile derived from interior models of Jupiter, constrained by a neural-network-based parameter sweep (53, 54). We focus here on the two lowest modes ($n = \{0, 1\}$), which are illustrated in Fig. 3 A and D). The $n = 0$ mode corresponds to a simple decay profile, whereas $n = 1$ changes sign along the column. This focus on the two leading modes aligns with estimates from Earth's oceans, where they capture the bulk of the kinetic energy (52, 56); higher modes require excitations with elaborate vertical profiles.

Since Eq. **6** depends only on H and N (here assumed constant, see discussion in *SI Appendix*), we present $L_{d,(n)}$ solutions as a function of these two parameters in Fig. 3 B and E, for both modes. The constrained range of deformation radii from the previous section (Fig. 2K) is indicated for the north (blue) and south (orange) poles, essentially giving an H as a function of N for each pole. Focusing on the relationship defined by the blue solid curve in Fig. 3 B and E, we plot the corresponding $\Phi_n(z)$ profiles as a function of pressure below the cloud level for different N values (Fig. 3 C and F).

Interestingly, in agreement with the eigenvalue results, the H vs. N line in Fig. 3C closely follows a scaling law derived for the aspect ratio of vortices in stratified fluids, supported by theory and rotating tank experiments (55, 57, 58). This vertical scaling, $H \sim f_0 R\sqrt{\mathrm{Ro}\,(1-\mathrm{Ro})\,/\,(N_c^2 - N^2)}$, can be simplified in our case to $H \sim f_0 R\sqrt{\mathrm{Ro}}/N$. This approximation is valid under the assumptions that the Rossby number is small ($\mathrm{Ro} = U/(f_0 R) \ll 1$) and that the static stability at the vortex center is small ($N_c^2 \ll N^2$). Under these conditions, the simplified scaling (purple dashed line in Fig. 3C) provides a good match to the curve derived from the eigenvalue solutions for the North Pole.

The MWR instrument, expected to probe below Jupiter's clouds at the north pole in the near future, measures brightness temperature at six channels. The maximum sensitivity pressure levels for each MWR channel are marked by green dotted lines, with Channel 6 above the 1-bar level. For a plausible range $N = 3 - 20 \times 10^{-3}\mathrm{s}^{-1}$ (59), consistent with our reanalysis of Galileo probe data (*SI Appendix*, Fig. S5), and focusing first on mode 0 (Fig. 3C), we anticipate that the north polar cyclones' footprint will be visible in Channels 6 and 5 (and Channel 4 if $N \approx 3 \times 10^{-3}\mathrm{s}^{-1}$). However, if the real Jovian poles exhibit turbulence with a vertical phase shift, reminiscent of terrestrial storms with low-level convergence and upper-level divergence, then mode 1 may also be excited. In that scenario (Fig. 3F), signatures could extend into Channel 3 for the same range of Ns.

Fig. 4 illustrates an example of how ψ extends downward and intersects with the MWR channels for $N = 3 \times 10^{-3}\,\mathrm{s}^{-1}$, the lower bound estimated in ref. 59. Channel 6, sensitive to pressures around 0.7 bar, lies slightly above the eigenfunctions' range (which starts near 1 bar). We assume that Channel 6 will display a ψ field similar to that of Channel 5. The JIRAM background photograph (16) represents the cloud deck at approximately this pressure level. The downward extension of ψ below Channel 4 depends on the excitation of mode 1. It is important to note that the MWR measures brightness temperature, which is only indirectly related to ψ. Predicting MWR observations requires a layer of translation, involving solutions for vertical velocity and the subsequent diffusion-advection of ammonia, given the background ammonia distribution (13).

Discussion

In this study, we examined how the vertical extent of polar cyclones influences their vorticity-driven motion (Fig. 1). Our analysis demonstrated that shallower cyclones undergo a weaker β-drift, which explains the order-of-magnitude discrepancy

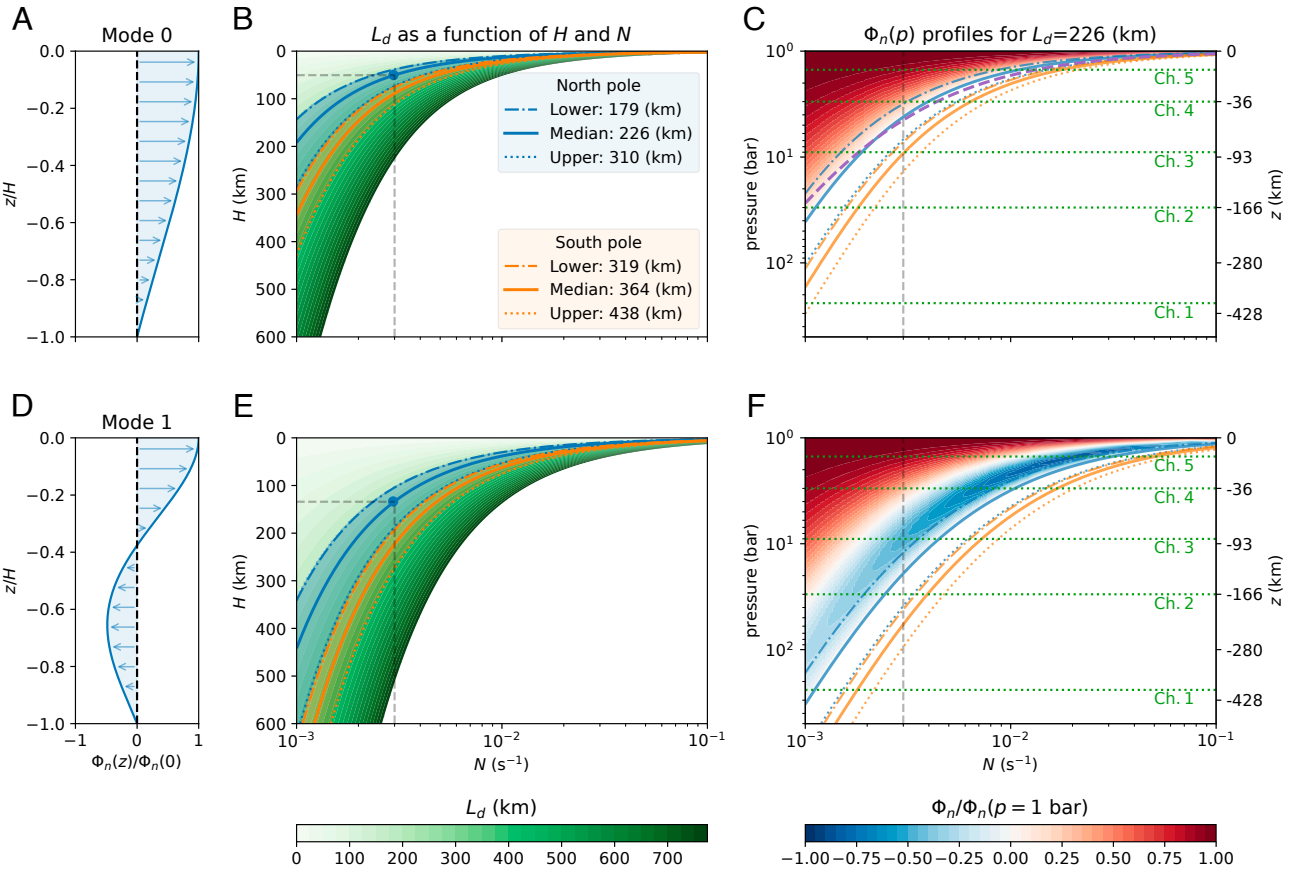

Fig. 3. Interpretation of the cyclones' vertical structure from the deformation radius. (*A*) Vertical profile of Φ_n for "mode 0". (*B*) Eigenvalue solutions for L_d (green shades) for various combinations of N (Brunt-Väisälä frequency) and H (depth) for mode 0. The estimated L_d distributions from Fig. 2*K* are shown by the blue and orange curves for the north and south poles, respectively. Values of L_d exceeding 800 km are not contoured for clarity. (*C*) Solutions for Φ_n as a function of pressure below the cloud layer, following the *N*-*H* relationship indicated by the blue solid curve in panel (*B*). Green horizontal dotted lines indicate the depths at which each MWR channel has maximum sensitivity (10), though each channel is sensitive over a broader range of depths. The numbers on the right ordinate show the altitude relative to 1 bar. (*D*-*F*) The same as (*A*-*C*) but for "mode 1". Gray dashed lines in panels (*B*, *C*, *E*, and *F*) denote the values used to generate the profiles in panels (*A* and *D*), and to produce Fig. 4. The color along the gray dashed line in panels (*C* and *F*) corresponds to the $\Phi(z)$ profiles shown in panels (*A* and *D*). The purple dashed line in panel (*C*) represents the theoretical scaling $H \sim \mathrm{Ro}^{1/2} R f_0 / N$ (adapted from ref. 55), using representative values of $R = 800$ km and $U = 90\,\mathrm{ms}^{-1}$ from Fig. 2 *M* and *N*.

between the observed westward drift of the south-polar cyclones and the much faster rates anticipated by an idealized, infinitely deep model [(29), their Fig. 2].

We then employed a 2D polar model initialized with identical cyclones at their observed locations (during PJ4). This model provides a dynamical constraint on the deformation radius, L_d (Fig. 2), which encodes information about the cyclones' vertical structure. We found that both excessively large and excessively small values of L_d produce westward drifts that deviate strongly from observations. A sampling algorithm estimates $L_d \sim 226$ (km) at the north pole and ~ 364 (km) at the south pole. While the posterior distributions of L_d at the two poles do overlap, it remains an open question whether genuine differences in L_d exist between the poles, especially given Jupiter's negligible obliquity and the resulting expected hemispheric symmetry. However, the indicated difference in L_d between the poles could have important implications for the characteristics of the polar cyclones. Since L_d controls the spatial scale of vortices in geostrophic turbulence (60), the possibly smaller L_d at the north pole may explain the greater number of smaller cyclones observed at the north pole compared to the south.

Using these estimates of L_d, we sought consistency between the 2D QG framework (Fig. 2) and a 3D QG model that incorporates density variations with depth (Eq. **4**). This required solving the eigenvalue problem in Eq. **6**, in which the eigenvalues yield L_d for different vertical modes, and the numerically determined eigenfunctions describe the cyclone's vertical structure relative to the cloud deck. In our idealized approach, we assumed a constant Brunt-Väisälä frequency, N, and a single dominant vertical mode, both of which can introduce uncertainty.

We emphasize that the eigenvalue-derived L_d represents a vertically integrated quantity that encapsulates, as accurately as possible, the effects of vertical stretching on 2D dynamics when density varies significantly with depth and the atmosphere is stably stratified. While the linear dynamics at the top layer ($z = 0$) of the 3D-QG model (Eq. **4**) and the 2D-QG model (Eq. **3**) are identical—for example, in a Rossby wave solution (46)—nonlinearities and multimodal dynamics introduce deviations between the models (*SI Appendix*). Quantifying this error is worthwhile but requires full 3D simulations at the pole with sufficient resolution, which is left for future work.

The solutions (Fig. 3) suggest that for $N \approx 10^{-2}\,\mathrm{s}^{-1}$, cyclone depths of 10 to 75 km at the north pole and 20 to 90 km at the south pole are plausible, depending on the mode.

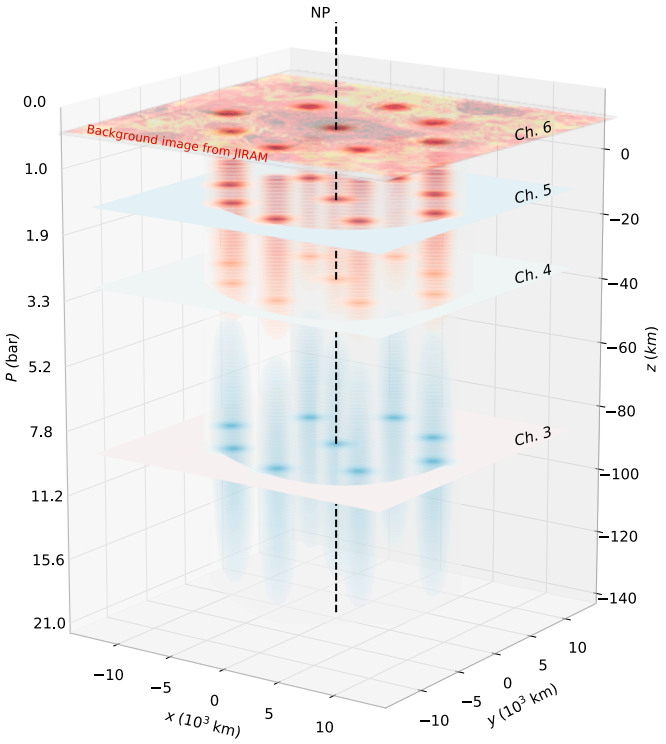

Fig. 4. Vertical structure and intersections with instrument sensitivity depths at the north pole. The ψ field from Fig. 2*C* was extended downward (rather than computed directly in a 3D simulation) using the eigenfunctions from Fig. 3 *A* and *D*, which correspond to $N = 3 \times 10^{-3}$ (s^{-1}) and $H = 50$ (133) km for mode 0 (mode 1). Both modes yield $L_d = 226$ km, with mode 0 terminating ($\psi = 0$) at $z = -50$ km, and mode 1 continuing further to $\psi = 0$ at $z = -134$ km. The planes represent ψ at the MWR channels that overlap with the eigenfunction range, while the shaded regions between the planes depict ψ values between the channels. The dashed black line indicates the north pole. The background image on channel 6 is a JIRAM measurement from PJ4 (16), similar to Fig. 2*A*.

If $N \approx 3 \times 10^{-3}\,s^{-1}$, the estimated cyclone depths increase substantially, ranging 30 to 220 km at the north pole and 60 to 330 km at the south pole. As a comparison, the GRS has been estimated to be approximately 300 ± 100 km deep based on gravity measurements (8), and its signature has been observed down to MWR channel 1, corresponding to depths of $O(300\,\text{km})$ (18), consistent with both experimental and numerical modeling results (58). Although the GRS is a distinct low-latitude anticyclone, these estimates suggest that the lower-N ($\sim 3 \times 10^{-3}\,s^{-1}$) regime considered here may provide a more realistic representation of Jupiter's deep vortices.

These results (Figs. 3 and 4) also establish a framework for interpreting forthcoming measurements from Juno's MWR at Jupiter's north pole (17). Once these measurements become available, our model can be used to connect each channel's footprint to the underlying vertical structure and static stability N. In a subsequent analysis, one can investigate how the cyclonic circulations drive vertical transport and ammonia redistribution, following an approach akin to that used in the study of Jupiter's Ferrel-cell circulation (13).

In summary, our work presents a framework connecting observed cloud-level motions to the deeper structure of Jovian polar cyclones. By linking the deformation radius, derived from β-drift constraints, to vertical modes in a 3D-QG framework, we gain insights into how these cyclones extend below the visible cloud layer and how their internal structure influences their horizontal drift. These constraints on deformation radius, static stability, and vertical profile can guide future studies aimed at modeling the energy fluxes responsible for the formation and maintenance of these cyclones against dissipation.

Data, Materials, and Software Availability. Previously published data were used for this work (29, 40).

ACKNOWLEDGMENTS. This research was supported by the Israeli Space Agency and the Helen Kimmel Center for Planetary Science at the Weizmann Institute of Science. We gratefully acknowledge Rei Chemke, Keren Duer, Eli Galanti, Gidi Yoffe, and Or Hadas for their insightful discussions and valuable feedback. We also thank the editor and two anonymous reviewers for constructive comments that improved this manuscript.

1. S. K. Atreya *et al.*, A comparison of the atmospheres of Jupiter and Saturn: Deep atmospheric composition, cloud structure, vertical mixing, and origin. *Planet. Space Sci.* **47**, 1243–1262 (1999).
2. I. de Pater, R. J. Sault, B. Butler, D. DeBoer, M. H. Wong, Peering through Jupiter's clouds with radio spectral imaging. *Science* **352**, 1198–1201 (2016).
3. R. E. Young, The Galileo probe mission to Jupiter: Science overview. *J. Geophys. Res. Planets* **103**, 22775–22790 (1998).
4. Y. Kaspi *et al.*, Jupiter's atmospheric jet streams extend thousands of kilometres deep. *Nature* **555**, 223–226 (2018).
5. E. Galanti *et al.*, Constraints on the latitudinal profile of Jupiter's deep jets. *Geophys. Res. Lett.* **48**, e2021GL092912 (2021).
6. Y. Kaspi *et al.*, Observational evidence for cylindrically oriented zonal flows on Jupiter. *Nat. Astron.* **7**, 1463–1472 (2023).
7. E. Galanti *et al.*, Determining the depth of Jupiter's Great Red Spot with Juno: A Slepian approach. *Astrophys. J.* **874**, L24 (2019).
8. M. Parisi *et al.*, The depth of Jupiter's Great Red Spot constrained by Juno gravity overflights. *Science* **374**, 964–968 (2021).
9. S. J. Bolton *et al.*, Jupiter's interior and deep atmosphere: The initial pole-to-pole passes with the Juno spacecraft. *Science* **356**, 821–825 (2017).
10. M. A. Janssen *et al.*, MWR: Microwave Radiometer for the Juno Mission to Jupiter. *Space Sci. Rev.* **213**, 139–185 (2017).
11. L. N. Fletcher *et al.*, Jupiter's temperate belt/zone contrasts revealed at depth by Juno microwave observations. *J. Geophys. Res. Planets* **126**, e2021JE006858 (2021).
12. C. Li *et al.*, The distribution of ammonia on Jupiter from a preliminary inversion of Juno microwave radiometer data. *Geophys. Res. Lett.* **44**, 5317–5325 (2017).
13. K. Duer *et al.*, Evidence for multiple Ferrel-like cells on Jupiter. *Geophys. Res. Lett.* **48**, e2021GL095651 (2021).
14. K. Duer, E. Galanti, Y. Kaspi, Gas giant simulations of eddy-driven jets accompanied by deep meridional circulation. *AGU Adv.* **4**, e2023AV000908 (2023).
15. A. Adriani *et al.*, JIRAM, the Jovian infrared auroral mapper. *Space Sci. Rev.* **213**, 393–446 (2017).
16. A. Adriani *et al.*, Clusters of cyclones encircling Jupiter's poles. *Nature* **555**, 216–219 (2018).
17. G. Orton *et al.*, "Unexpected results from microwave sounding of Jupiter's north polar cyclones". *Europlanet Science Congress*, EPSC2024-280 (2024).
18. S. J. Bolton *et al.*, Microwave observations reveal the deep extent and structure of Jupiter's atmospheric vortices. *Science* **374**, 968–972 (2021).
19. M. E. O'Neill, K. A. Emanuel, G. R. Flierl, Polar vortex formation in giant-planet atmospheres due to moist convection. *Nat. Geosci.* **8**, 523–526 (2015).
20. S. R. Brueshaber, K. M. Sayanagi, T. E. Dowling, Dynamical regimes of giant planet polar vortices. *Icarus* **323**, 46–61 (2019).
21. A. Hyder, W. Lyra, N. Chanover, R. Morales-Juberías, J. Jackiewicz, Exploring Jupiter's polar deformation lengths with high-resolution shallow water modeling. *Planet. Sci. J.* **3**, 166 (2022).
22. L. Siegelman *et al.*, Moist convection drives an upscale energy transfer at Jovian high latitudes. *Nat. Phys.* **18**, 357–361 (2022).
23. L. Siegelman, W. R. Young, A. P. Ingersoll, Polar vortex crystals: Emergence and structure. *Proc. Natl. Acad. Sci. U.S.A.* **119**, e2120486119 (2022).
24. G. G. Sutyrin, G. R. Flierl, Intense vortex motion on the beta plane: Development of the beta gyres. *J. Atmos. Sci.* **51**, 773–790 (1994).
25. J. L. Franklin, S. E. Feuer, J. Kaplan, S. D. Aberson, Tropical cyclone motion and surrounding flow relationships: Searching for beta gyres in omega dropwindsonde datasets. *Mon. Weather. Rev.* **124**, 64–84 (1996).
26. J. Adem, A series solution for the barotropic vorticity equation and its application in the study of atmospheric vortices. *Tellus* **8**, 364–372 (1956).
27. R. K. Smith, W. Ulrich, An analytical theory of tropical cyclone motion using a barotropic model. *J. Atmos. Sci.* **47**, 1973–1986 (1990).
28. J. S. L. Lam, D. G. Dritschel, On the beta-drift of an initially circular vortex patch. *J. Fluid Mech.* **436**, 107–129 (2001).
29. N. Gavriel, Y. Kaspi, The westward drift of Jupiter's polar cyclones explained by a center-of-mass approach. *Geophys. Res. Lett.* **50**, e2023GL103635 (2023).
30. E. Firing, R. C. Beardsley, The behavior of a barotropic eddy on a β-plane. *J. Phys. Oceanogr.* **6**, 57–65 (1976).
31. G. F. Carnevale, R. C. Kloosterziel, G. J. F. Van Heijst, Propagation of barotropic vortices over topography in a rotating tank. *J. Fluid Mech.* **233**, 119–139 (1991).
32. A. Stegner, V. Zeitlin, From quasi-geostrophic to strongly nonlinear monopolar vortices in a paraboloidal shallow-water-layer experiment. *J. Fluid Mech.* **356**, 1–24 (1998).

33. J. B. Flór, I. Eames, Dynamics of monopolar vortices on a topographic beta-plane. *J. Fluid Mech.* **456**, 353–376 (2002).
34. D. Benzeggouta, B. Favier, M. Le Bars, Laboratory model for barotropic vortices drifting towards a planetary pole. *Phys. Rev. Fluids* **10**, 014701 (2025).
35. N. Gavriel, Y. Kaspi, The number and location of Jupiter's circumpolar cyclones explained by vorticity dynamics. *Nat. Geosci.* **14**, 559–563 (2021).
36. C. Li, A. P. Ingersoll, A. P. Klipfel, H. Brettle, Modeling the stability of polygonal patterns of vortices at the poles of Jupiter as revealed by the Juno spacecraft. *Proc. Natl. Acad. Sci. U.S.A.* **117**, 24082–24087 (2020).
37. N. Gavriel, Y. Kaspi, The oscillatory motion of Jupiter's polar cyclones results from vorticity dynamics. *Geophys. Res. Lett.* **49**, e2022GL098708 (2022).
38. A. Mura *et al*., Oscillations and stability of the Jupiter polar cyclones. *Geophys. Res. Lett.* **48**, e2021GL094235 (2021).
39. A. Adriani *et al*., Two-year observations of the Jupiter polar regions by JIRAM on board Juno. *J. Geophys. Res. Planets* **125**, e2019JE006098 (2020).
40. A. Mura *et al*., Five years of observations of the circumpolar cyclones of Jupiter. *J. Geophys. Res. Planets* **127**, e2022JE007241 (2022).
41. R. K. Smith, An analytic theory of tropical-cyclone motion in a barotropic shear flow. *Q. J. R. Meteorol. Soc.* **117**, 685–714 (1991).
42. S. G. L. Smith, The motion of a non-isolated vortex on the beta-plane. *J. Fluid Mech.* **346**, 149–179 (1997).
43. J. C. L. Chan, R. T. Williams, Analytical and numerical studies of the beta-effect in tropical cyclone motion. Part I: Zero mean flow. *J. Atmos. Sci.* **44**, 1257–1265 (1987).
44. K. J. Burns, G. M. Vasil, J. S. Oishi, D. Lecoanet, B. P. Brown, Dedalus: A flexible framework for numerical simulations with spectral methods. *Phys. Rev. Res.* **2**, 023068 (2020).
45. J. Buchner, Ultranest–a robust, general purpose Bayesian inference engine. arXiv [Preprint] (2021). http://arxiv.org/abs/2101.09604 (Accessed 17 September 2024).
46. G. K. Vallis, *Atmospheric and Oceanic Fluid Dynamics* (Cambridge University Press, 2017).
47. J. H. Rogers *et al*., Flow patterns of Jupiter's south polar region. *Icarus* **372**, 114742 (2022).
48. G. S. Orton *et al*., The first close-up images of Jupiter's polar regions: Results from the Juno mission JunoCam instrument. *Geophys. Res. Lett.* **44**, 4599–4606 (2017).
49. J. Buchner, Nested sampling methods. *Stat. Surv.* **17**, 169–215 (2023).
50. D. Grassi *et al*., First estimate of wind fields in the Jupiter polar regions from JIRAM-Juno images. *J. Geophys. Res. Planets* **123**, 1511–1524 (2018).
51. T. Guillot, P. Morel, CEPAM: A code for modeling the interiors of giant planets. *Astron Astro Supp. ser.* **109**, 109–123 (1995).
52. K. S. Smith, G. K. Vallis, The scales and equilibration of midocean eddies: Freely evolving flow. *J. Phys. Oceanogr.* **31**, 554–571 (2001).
53. M. Ziv, E. Galanti, S. Howard, T. Guillot, Y. Kaspi, Characterizing Jupiter's interior using machine learning reveals four key structures. *Astron. Astrophys.* **692**, A251 (2024).
54. M. Ziv *et al*., NeuralCMS: A deep learning approach to study Jupiter's interior. *Astron. Astrophys.* **686**, L7 (2024).
55. O. Aubert, M. Le Bars, P. Le Gal, P. S. Marcus, The universal aspect ratio of vortices in rotating stratified flows: Experiments and observations. *J. Fluid Mech.* **706**, 34–45 (2012).
56. R. Ferrari, C. Wunsch, The distribution of eddy kinetic and potential energies in the global ocean. *Tellus A* **62**, 92–108 (2010).
57. P. Billant, J. M. Chomaz, Self-similarity of strongly stratified inviscid flows. *Phys. Fluids* **13**, 1645–1651 (2001).
58. D. Lemasquerier, G. Facchini, B. Favier, M. Le Bars, Remote determination of the shape of Jupiter's vortices from laboratory experiments. *Nat. Phys.* **16**, 695–700 (2020).
59. S. Lee, Y. Kaspi, Towards an understanding of the structure of Jupiter's atmosphere using the ammonia distribution and the transformed Eulerian mean theory. *J. Atmos. Sci.* **78**, 2047–2056 (2021).
60. L. M. Polvani, J. C. McWilliams, M. A. Spall, R. Ford, The coherent structures of shallow-water turbulence: Deformation-radius effects, cyclone/anticyclone asymmetry and gravity-wave generation. *Chaos* **4**, 177–186 (1994).